ACS APPLIED MATERIALS & INTERFACES

Research Article

Cite This: ACS Appl. Mater. Interfaces 2019, 11, 4983−4994

www.acsami.org

Hierarchically Structured $Co(OH)_2$/CoPt/N-CN Air Cathodes for Rechargeable Zinc−Air Batteries

Kai Wang,[†] Wen Wu,[†] Zhenghua Tang,*[,†,‡] Ligui Li,[†] Shaowei Chen,[†,§] and Nicholas M. Bedford*[,∥]

[†]Guangzhou Key Laboratory for Surface Chemistry of Energy Materials and New Energy Research Institute, School of Environment and Energy, and [‡]Guangdong Engineering and Technology Research Center for Surface Chemistry of Energy Materials, South China University of Technology, Guangzhou Higher Education Mega Centre, Guangzhou 510006, China

[§]Department of Chemistry and Biochemistry, University of California Santa Cruz, 1156 High Street, Santa Cruz, California 95064, United States

[∥]School of Chemical Engineering, University of New South Wales, High Street, Sydney, New South Wales 2052, Australia

Supporting Information

ABSTRACT: For the realization of the large-scale deployment of rechargeable Zn−air batteries, it is crucial to develop cost-effective, efficient, and stable bifunctional electrocatalysts for both oxygen reduction reaction (ORR) and oxygen evolution reaction (OER). In this work, an integrated electrocatalyst consisting of $Co(OH)_2$/CoPt/N-CN was developed to enable both ORR and OER reactions for Zn−air batteries. The hierarchical $Co(OH)_2$/CoPt/N-CN electrocatalyst has desirable electrochemical properties, with comparable activity and better durability than commercial Pt/C for ORR and improved activity and long-term stability than commercial IrO_2 catalyst for OER. When implemented as air−cathode for rechargeable Zn−air batteries, $Co(OH)_2$/CoPt/N-CN exhibited a high power-density of 171 mW cm^{-2}, a specific capacity of 812 mA h g^{-1}, and a robust cycling life. Interestingly, the hierarchical structure remained intact upon charge and discharge tests, suggesting potential long-term use in the Zn−air battery technology. The material development strategy presented here can enrich the toolbox for the design and construction of cost-effective, efficient, and robust bifunctional electrocatalysts for ORR and OER toward rechargeable Zn−air battery applications.

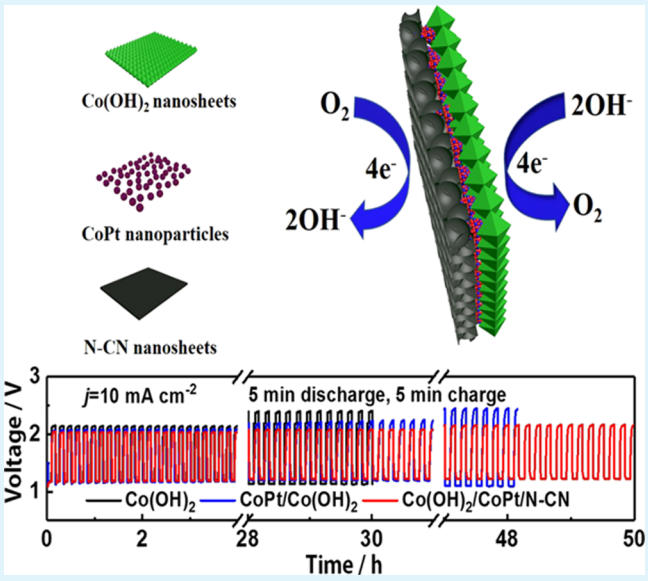

KEYWORDS: *$Co(OH)_2$/CoPt/N-CN, bifunctional electrocatalyst, hierarchical structure, oxygen evolution reaction, oxygen reduction reaction, rechargeable zinc−air batteries*

1. INTRODUCTION

The global increasing energy demand has driven the rapid development of alternative energy harvesting and conversion devices that require meaningful energy storage solutions with high energy densities. Rechargeable Zn−air batteries are currently attracting worldwide attention because of their low-cost, high theoretical energy density (1084 W h kg^{-1}), and safe operation.[1−3] The electrochemical reactions of rechargeable Zn−air battery in alkaline electrolyte can be summarized by their discharging and charging reactions. During discharging, the Zn electrode is oxidized to ZnO while O_2 is reduced [oxygen reduction reaction (ORR)]. Conversely, the charging process involves that the ZnO on the negative electrode is reduced to zinc while the hydroxyl ions on the positive electrode is oxidized to oxygen [oxygen evolution reaction (OER)].[4] These reactions are summarized as follows

$$\text{Zinc electrode: } 2Zn + 4OH^- \underset{\text{charge}}{\overset{\text{discharge}}{\rightleftharpoons}} 2ZnO + 2H_2O + 4e^-$$

$$\text{Air electrode: } O_2 + 4e^- + 2H_2O \underset{\text{charge}}{\overset{\text{discharge}}{\rightleftharpoons}} 4OH^-$$

Received: October 22, 2018
Accepted: January 8, 2019
Published: January 9, 2019

DOI: 10.1021/acsami.8b18424
ACS Appl. Mater. Interfaces 2019, 11, 4983−4994

$$\text{Overall reaction: } 2Zn + O_2 \underset{\text{charge}}{\overset{\text{discharge}}{\rightleftharpoons}} 2ZnO$$

OER and ORR are the two key reactions occurring at the cathode of rechargeable Zn−air battery, which represents the charging and discharging process, respectively.[5,6] To date, a large overpotential is required for OER and ORR and thus must be remarkably decreased for Zn−air batteries to serve as meaningful energy storage devices.[7] Moreover, the current commercial standard electrocatalysts for OER and ORR still rely on noble metal-based materials (e.g., IrO_2/RuO_2 for OER, Pt for ORR). Aside from obvious cost/scarcity issues, these catalysts are also plagued with inefficient activity and undesirable long-term stability.[8] Therefore, to realize the commercialization of next-generation rechargeable Zn−air batteries, developing a dual-functional electrocatalyst with high stability, excellent activity, and low cost is imperative.[9−11]

Recently, layered double hydroxides (LDHs) consisting of inexpensive metals have emerged as an alternative candidate to replace Ir/Ru-based catalysts for OER because of their excellent OER activity and ease of large-scale accessibility. For instance, Fan et al. reported a monolayer of nickel−vanadium-LDH (NiV LDH) that showed a current density of 27 mA cm^{-2} at an overpotential of 350 mV for water oxidation.[12] By employing a one-pot coprecipitation method at room temperature, ultrathin nanoplates of cobalt−manganese LDH (CoMn LDH) was fabricated by Song and Hu, and such LDH exhibited 9 times higher than the TOF of a precious IrO_2 catalyst for OER.[13] Tang and Guo group developed a novel and straightforward strategy to fabricate Ni−Co double hydroxides nanocages, where reactivity to OER could be altered by optimizing the Ni−Co composition.[14] Such LDHs often displayed excellent OER activity that surpasses the performance of IrO_2 catalysts.[15−17] However, the inclusion of LDHs as Zn−air battery catalysts failed to achieve satisfactory discharge performance, mainly because of their limited ORR activity.[18,19] In this regard, Pt-based materials are still the commercial standard for ORR, yet there is a strong push away from Pt-based materials to lower cost while trying to improve/maintain the intrinsic activity of Pt.[20,21] To this end, one effective approach is to alloy Pt with 3d transition metals.[22] Stamenkovic et al. demonstrated that alloying Pt with 3d transition metals can tune its electronic structure and consequently enhances its performance toward ORR.[23] For example, PtCo electrocatalysts have been demonstrated to possess superior ORR activity and markedly higher long-term durability than commercial Pt/C catalyst.[24−26] As such, coupling layered hydroxide with PtCo as a hierarchical electrocatalysts is expected to endow both advantageous OER and ORR performance toward Zn−air battery applications. To further improve the electric conductivity and provide additional electrochemically active sites, a hierarchical electrocatalyst consisting of nitrogen-doped porous carbon nanosheets (N-CN) is desirable, as N-CN can be introduced as the support. N-CN possessed high surface area, excellent conductivities, and abundant active sites for electrocatalytic reactions.[27,28] The most critical feature related to the electrocatalytic activity of N-CN is the charge delocalization of the carbon skeleton induced by nitrogen doping, which results in the nonelectroneutrality of the catalysts and consequently facilitates oxygen adsorption and reduction.[29] By hierarchically combining material components that exhibit desirable OER and ORR activity and are electrically conductive, new electrocatalysts for Zn−air batteries can be obtained which may also enable synergistic properties enhancements.

Herein, we developed a facile strategy to integrate layered $Co(OH)_2$ with CoPt nanoparticles and N-CNs in a hierarchical fashion with desirable electrocatalytic properties for Zn−air batteries. The $Co(OH)_2$/CoPt/N-CN electrocatalysts were found to have a well defined hierarchical structure through various characterization methods. Electrocatalytic tests indicated that its ORR activity was comparable with Pt/C catalyst along with outperformed durability, while its OER activity and long-term stability was superior than IrO_2 catalyst. The inclusion of $Co(OH)_2$/CoPt/N-CN as air−cathode in a rechargeable Zn−air battery resulted in a high power-density, capacity, and long cycling life. Furthermore, the well-defined hierarchical structure remained intact after long cycles of charge−discharge process.

2. RESULTS AND DISCUSSION

2.1. Preparation and Structural Characterizations of the $Co(OH)_2$/CoPt/N-CN. The typical preparation procedure of the resulting catalysts is depicted in Scheme 1. Briefly, NaCl

Scheme 1. Schematic for the Preparation of the $Co(OH)_2$/CoPt/N-CN Composite

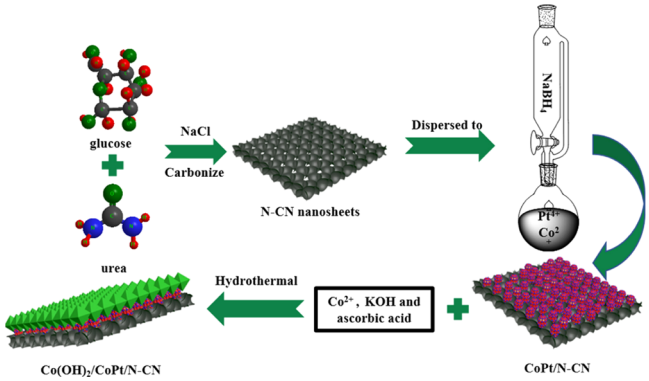

was first added into a urea (as the nitrogen source) and glucose (as the carbon skeleton) solution. After lyophilization, the mixture formed a resin by polycondensation and with NaCl as the template, which then evolved into the nitrogen-doped carbon nanosheets during the carbonizing process in Ar atmosphere. CoPt/N-CN formed is formed by replacing NaCl with Pt^{4+} and Co^{2+} ions into the solution, following by reduction through $NaBH_4$. Finally, KOH and L-ascorbic acid (LAA) were added into the solution to synthesize $Co(OH)_2$, where LAA serves as a morphology-directing agent. The OH^- ions first reacted with LAA leading to the formation of L-dehydroascorbic acid (DAA) through the reaction LAA + $OH^- \rightarrow$ DAA + H_2O. With the presence of Co^{2+} ions, small $Co(OH)_2$ nanosheet seeds can easily form. Driven by DAA, such small $Co(OH)_2$ nanosheet seeds can further experience an epitaxial lateral overgrowth process, and finally evolved into thin nanosheets and covered onto CoPt/N-CN to eventually form a sandwich-like structure of $Co(OH)_2$/CoPt/N-CN.[30]

The morphology and surface structure of the samples were first observed by scanning electron microscopy (SEM). As shown in Figure 1a,b, N-CN and $Co(OH)_2$ exhibited a thin sheet structure that is a vital prerequisite for preparing the hierarchical structure of $Co(OH)_2$/CoPt/N-CN. The typical

DOI: 10.1021/acsami.8b18424
ACS Appl. Mater. Interfaces 2019, 11, 4983−4994

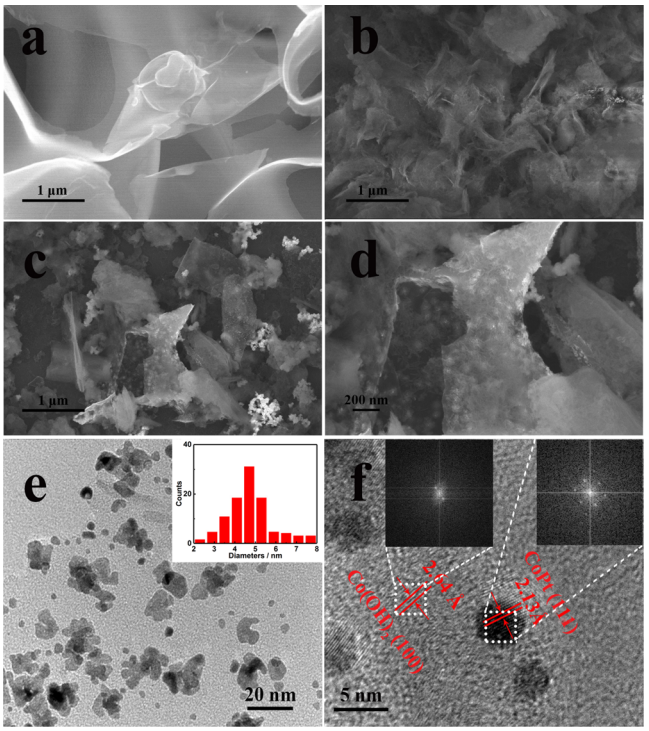

Figure 1. Representative SEM images of (a) N-CN, (b) $Co(OH)_2$, (c,d) $Co(OH)_2$/CoPt/N-CN, while (e,f) are the representative TEM images of $Co(OH)_2$/CoPt/N-CN with different magnifications. The inset in (e) is the size distribution histogram of CoPt nanoparticles and the inset in (f) is the FFT patterns for $Co(OH)_2$ and CoPt.

SEM image of CoPt/N-CN can be found in Figure S1, where CoPt nanoparticles lie on the surface of N-CN. Figure 1c shows the morphology of the $Co(OH)_2$/CoPt/N-CN, where it exhibits a foam-like structure. The representative high-magnification SEM image is presented in Figure 1d, and it can be noted that the foam-like structure consists of a variety of morphologies including sheets, spheres, and flakes. These three-dimensional architectures yield highly accessible active sites along with a high surface area to maximize mass transport conduction for electrocatalytic reactions.[31,32] Moreover, the representative high-resolution transmission electron microscopy (HRTEM) images and corresponding fast Fourier transform (FFT) patterns of $Co(OH)_2$/CoPt/N-CN are shown in Figure 1e,f. It can be noted that, there are several CoPt nanoparticles building blocks with size approximately of 10−20 nm on the surface of N-CN (Figure 1e). Each building block may contain several CoPt nanocrystals, and based on more than 100 individual nanocrystals, the average diameter of CoPt nanocrystals is 4.70 ± 1.75 nm (inset in Figure 1e). A lattice spacing of 2.13 and 2.64 Å can be easily identified in Figure 1f and the insert FFT patterns which are ascribed to the CoPt(111)[33] and $Co(OH)_2$(100) planes,[34] respectively. Both CoPt nanoparticles and $Co(OH)_2$ nanosheets lie onto the surface of N-CN, some CoPt nanoparticles might be covered by $Co(OH)_2$, suggesting the formation of a hierarchical structure which likely have implications for electrocatalytic properties. Moreover, the surface area and pore size distribution measured by Brunauer−Emmett−Teller (BET) can be found in Figure S2. All of the N_2 adsorption−desorption isotherms exhibited a type-IV isotherm with a H3-type hysteresis loop, suggesting disordered slit and wedge shape pores are probably stacked between the lamellar materials. The BET pattern agrees well with the SEM features, further confirming that the hierarchical structure of $Co(OH)_2$/CoPt/N-CN was successfully obtained. The BET surface area of N-CN was calculated to be 223 $m^2\ g^{-1}$, larger than that of CoPt/N-CN (118 $m^2\ g^{-1}$), indicating that CoPt nanoparticles have been adsorbed into the pores of N-CN. Interestingly, once $Co(OH)_2$ was covered on CoPt/N-CN, the specific

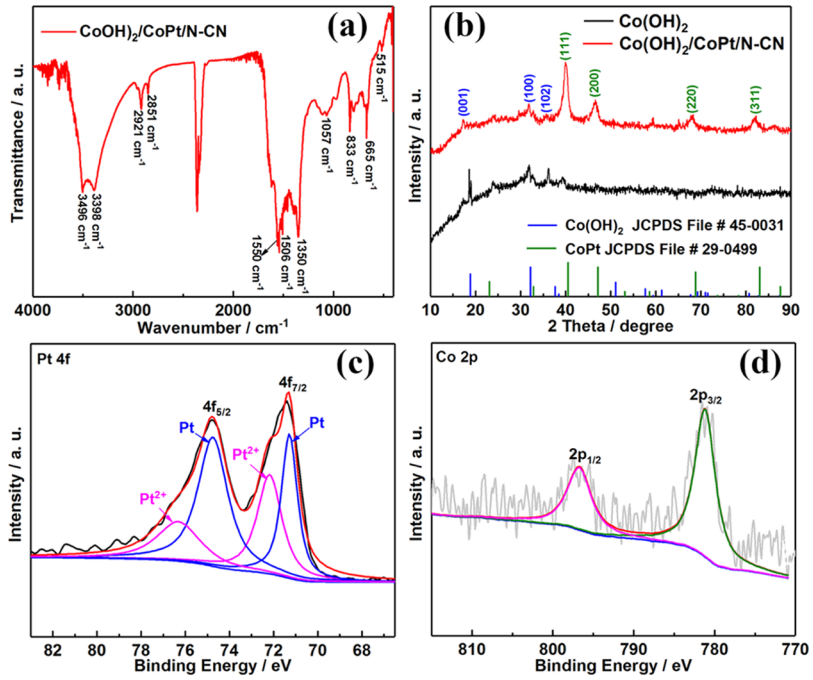

Figure 2. (a) FT-IR spectra of $Co(OH)_2$/CoPt/N-CN, (b) XRD patterns of $Co(OH)_2$/CoPt/N-CN and $Co(OH)_2$, the core-level XPS spectra of (c) Pt 4f electrons and (d) Co 2p electrons for the $Co(OH)_2$/CoPt/N-CN sample. Black lines correspond to the XPS data and red lines are the fitted curves.

DOI: 10.1021/acsami.8b18424
ACS Appl. Mater. Interfaces 2019, 11, 4983−4994

surface area of $Co(OH)_2$/CoPt/N-CN increased to 178 $m^2 g^{-1}$, which can be attributed to the contribution from $Co(OH)_2$. Additionally, the energy-dispersive system spectrum of $Co(OH)_2$/CoPt/N-CN can be found in Figure S3, where the weight percentage of each element can be quantified. From the inset pie chart, it can be noted that, C is over 50%, O is over 20%, while Co and Pt are only 11.46 and 9.23%, respectively.

Figure 2a shows the Fourier-transform infrared spectroscopy (FT-IR) spectra of the $Co(OH)_2$/CoPt/N-CN in the wavenumber range of 400−4000 cm^{-1}. The twin peaks at 3496 and 3398 cm^{-1} can be assigned to the stretching vibrations of hydrogen-bond from hydroxyl groups (−OH) in the $Co(OH)_2$ and adsorbed water.[35,36] A couple of vibration bands located at 2921 and 2851 cm^{-1} can be associated with the C−H antisymmetric stretching and symmetric stretching. The peaks at 1550, 1506, 1350, 1057, and 833 cm^{-1} are attributed to the (C−N) stretching vibration, (C−H) bending vibration, (CH_3) symmetrical deformation, (C−O) skeletal stretching vibration, and (CO_3) scissoring vibration, respectively.[35−37] Furthermore, the Co−OH stretching vibration can be observed at 515 cm^{-1}.[38] As a comparison, the peaks of −OH vibration at 3496 and 515 cm^{-1} are absent for the CoPt/N-CN and N-CN samples (Figure S4). The above characteristic peaks in FT-IR confirmed that $Co(OH)_2$, CoPt, and N-CN were well integrated and a composite sample of $Co(OH)_2$/CoPt/N-CN was formed. The Raman spectra of N-CN are shown in Figure S5, where the typical D and G bands are observed at 1360 and 1557 cm^{-1}, respectively. The intensity ratio of D band to G band (I_D/I_G) can be used to evaluate the degree of defect and disordered structures.[39] Given the I_D/I_G ratio for N-CN is 1.02, a highly defective structure is likely for N-CN. The crystalline phase of $Co(OH)_2$ and $Co(OH)_2$/CoPt/N-CN were then detected by X-ray diffraction (XRD) measurements. As shown in Figure 2b, the diffraction peaks at 18.6° and 17.4° can be assigned to the (001) planes of $Co(OH)_2$ nanosheets (JCPDS file no. 45-0031), whereas the peaks at 40.0°, 46.6°, 68.0°, and 82.0° correspond well with (111), (200), (220), and (311) planes of CoPt nanoparticles (JCPDS file no. 29-0499), respectively.[34] In comparison to $Co(OH)_2$, the $Co(OH)_2$/CoPt/N-CN(001) plane slightly left shifted, as an indicative of interlayer spacing expansion.[40] Note that, it has been demonstrated that the interlayer expansion of layered structures for cobalt hydroxide could substantially enhance the OER catalytic performance.[40]

The elemental composition and chemical valence state of $Co(OH)_2$/CoPt/N-CN was subsequently investigated by X-ray photoelectron spectra (XPS) measurements. The high-resolution XPS spectra of Pt 4f and Co 2p electrons are presented in Figure 2c,d. As shown in Figure 2c, the core-level spectra of the Pt 4f (Figure 2c) electrons exhibit two peaks, which can be further deconvoluted into two doublets. The peaks with binding energies at 71.27 and 74.78 eV can be ascribed to metallic platinum, while the other two peaks at 72.19 and 76.36 eV belong to Pt^{2+} ions from PtO.[26] On the basis of the integrated peak area, Pt(0) is dominant in the Pt species. As a note, Pt(0) can afford more appropriate active sites for ORR than Pt^{2+}.[41] The core-level XPS spectra of Co 2p electrons is presented in Figure 2d. The peaks with binding energy at 781.0 and 796.9 eV can be attributed to the Co $2p_{3/2}$ and Co $2p_{1/2}$ electrons, respectively. The binding energy gap between the Co $2p_{3/2}$ and Co $2p_{1/2}$ electrons reached a value as large as 15.9 eV, which is a characteristic signature for the $Co(OH)_2$ with laminar structure.[42] It further confirms that the $Co(OH)_2$ nanosheets were likely lying onto the surface of CoPt/N-CN, which could play a role in electrocatalytic properties.

2.2. Electrocatalytic Performance. The electrocatalytic performance toward ORR and OER were first studied by linear scanning voltammetry (LSV). As presented in Figure 3a, the

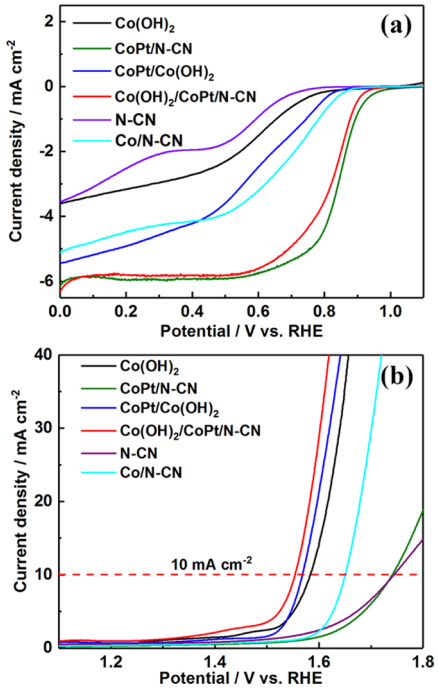

Figure 3. Polarization curves of the samples (a) ORR at 1600 rpm in O_2-saturated 0.1 mol L^{-1} KOH solution, (b) OER at 1600 rpm in 1 mol L^{-1} KOH solution.

$Co(OH)_2$ nanosheets and N-CN exhibited insufficient ORR activities. With $Co(OH)_2$ as the substrate, CoPt nanoparticles supported on $Co(OH)_2$ ($CoPt/Co(OH)_2$) still displayed an undesirable ORR activity, likely because of the possible coverage of hydroxide material on the bimetallic electrocatalyst. Although Co/N-CN exhibits fair ORR performance, the activity is not that desirable for Zn−air battery applications. Excellent functionalities toward both OER and ORR is the prerequisite for engineering catalyst toward Zn−air battery. To that end, both $Co(OH)_2$ and $CoPt/Co(OH)_2$ are not suitable as air−cathode for Zn−air battery. Interestingly, CoPt/N-CN and $Co(OH)_2$/CoPt/N-CN exhibited markedly superior ORR performance and showed an onset potential of 0.97 and 0.94 V, respectively. Such close onset potential, along with almost identical diffusion-limited current densities, indicates that the two samples possessed good and comparable ORR activities attributed to the alloyed CoPt nanoparticles, as well as, the well-defined porous structure of N-CN, as the substrate can prevent the coalescence, aggregation of the CoPt nanoparticles, and boost the local oxygen concentration on the surface of the CoPt nanoparticles.[26] The OER polarization curves are presented in Figure 3b. To afford a current density of 10 mA cm^{-2}, the required overpotential (shown in Table S1) was 510 mV for CoPt/N-CN, 510 mV for N-CN, 420 mV for Co/N-CN, 350 mV for $Co(OH)_2$, 340 mV for $CoPt/Co(OH)_2$, and 320 mV for $Co(OH)_2$/CoPt/N-CN. $Co(OH)_2$/CoPt/N-CN possessed the best OER activity among the series, while

DOI: 10.1021/acsami.8b18424
ACS Appl. Mater. Interfaces 2019, 11, 4983−4994

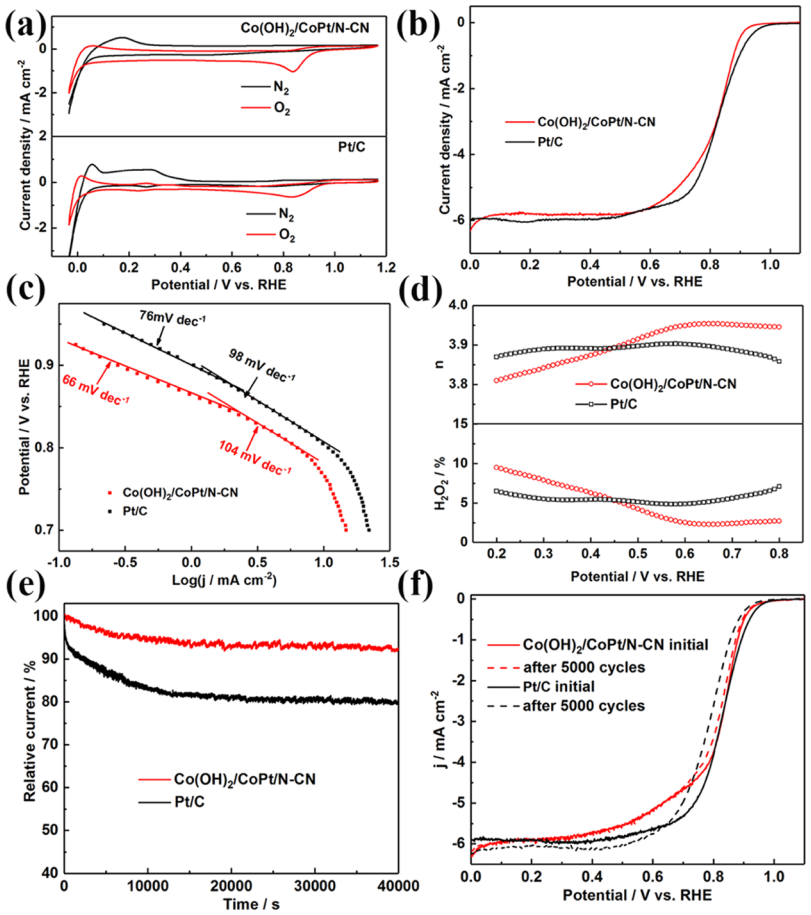

Figure 4. Electrocatalytic ORR performance of $Co(OH)_2$/CoPt/N-CN and Pt/C catalysts, (a) CVs in N_2− and O_2− saturated 0.1 mol L^{-1} KOH electrolyte at the scan rate of 10 mV s^{-1}, (b) polarization curves in O_2-saturated 0.1 mol L^{-1} KOH with 1600 rpm at 10 mV s^{-1}, (c) Corresponding Tafel plots, (d) Electron-transfer numbers and yields of H_2O_2 at different potentials, (e) *i*−*t* chronoamperometric response at the potential of 0.8 V and (f) ORR polarization curves of before and after 5000 cycles of cyclic voltammetric scans with potential range of 0.5−1.0 V in O_2-saturated 0.1 mol L^{-1} KOH solution at a scan rate of 50 mV s^{-1}.

$Co(OH)_2$ also demonstrated excellent OER performance. Note that, previous investigations have documented that such OER activity for LDH including $Co(OH)_2$ can be attributable to its multifarious chemical composition and unique two-dimensional laminar structures.[43,44]

By keeping the amount of CoPt nanoparticles constant (10%), we further attempted to optimize the ratio of $Co(OH)_2$-to-N-CN. As shown in Figure S6 and Table S1, when the mass ratio of N-CN decreased to 20% [the mass ratio of $Co(OH)_2$ increased to 70% correspondingly], the OER activity was lower than the originally discussed material [mass ratio of N-CN-to-$Co(OH)_2$ is 45%:45%], while the onset potential for ORR significantly shifted negatively. Conversely, when the mass ratio of N-CN increased to 70% [the mass ratio of $Co(OH)_2$ decreased to 20% correspondingly], the required overpotential at 10 mA cm^{-2} for OER increased drastically to 380 mV, albeit the onset potential for ORR was slightly positive than the original sample. In addition, we also explored the ORR and OER performance of the physical mixture of $Co(OH)_2$, CoPt, and N-CN. The polarization curve (Figures S7a and S8a) indicated that the ORR and OER activities of the physical mixture is not comparable with $Co(OH)_2$/CoPt/N-CN through hydrothermal treatment. The durability (Figures S7b and S8b) of the mixture is also very low, as the ORR and OER current decayed to 80 and 55% of its initial value after 8.3 h, respectively. This is likely because the physical mixture could not form a steady hierarchical structure.

The ORR performance of the $Co(OH)_2$/CoPt/N-CN sample was further examined and compared with the commercial Pt/C catalyst (Figure 4). As shown in Figure 4a, in N_2-saturated 0.1 M KOH solution, no redox peak can be observed for both $Co(OH)_2$/CoPt/N-CN and Pt/C. In O_2-saturated 0.1 M KOH, an obvious cathodic peak at about 0.84 V appeared for both samples, as expected. From the LSV curves in Figure 4b, the onset potential of $Co(OH)_2$/CoPt/N-CN can be estimated as 0.94 V, slightly lower than that of Pt/C (0.97 V). However, $Co(OH)_2$/CoPt/N-CN possessed the identical half-wave potential value (0.83 V) with the Pt/C catalyst. Subsequently, the LSV measurements at different rotation rates from 400 to 2500 rpm were conducted and presented in Figure S9. The inset Koutecky−Levich plots in Figure S9 exhibited a highly linear trend, suggesting that a first reaction kinetics with regard to oxygen concentration in the solution was adopted. Further reaction insights can be acquired by analyzing the Tafel plots, where corresponding Tafel slopes can be extrapolated (Figure 4c). It should be noted that the Tafel plots displayed two linear regions at low and high overpotentials, where such a phenomenon has been described in several previous reports.[26,45,46] In the low overpotential range, the slope was calculated to be 66 and 76 mV dec^{-1} for $Co(OH)_2$/CoPt/N-CN and Pt/C, respectively. The value for

DOI: 10.1021/acsami.8b18424
ACS Appl. Mater. Interfaces 2019, 11, 4983−4994

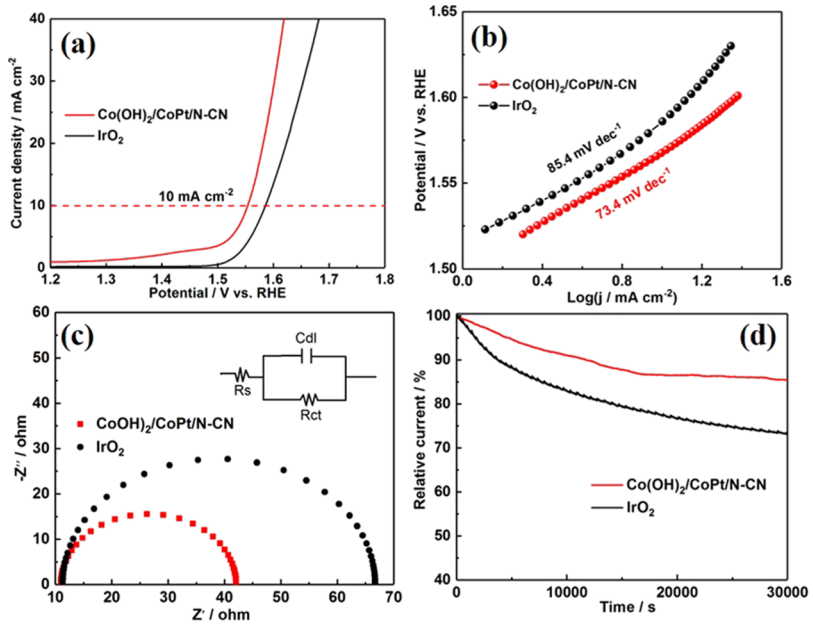

Figure 5. OER performance of $Co(OH)_2$/CoPt/N-CN and IrO_2 catalysts in N_2-saturated 1 mol L^{-1} KOH electrolyte, (a) polarization curves with the rotating speed of 1600 rpm, (b) corresponding Tafel plots, (c) Nyquist plots of the impedance and (d) *i*−*t* chronoamperometric response at the potential of 1.55 V.

$Co(OH)_2$/CoPt/N-CN is smaller than that of Pt/C but close to 60 mV dec^{-1}, suggesting that the rate determining step during the ORR process is probably a pseudo two-electron reaction.[47−49] While in the high overpotential range, the slope was 98 and 104 mV dec^{-1} for Pt/C and $Co(OH)_2$/CoPt/N-CN, respectively. It indicates that the reaction rate was predominantly governed by the first electron transfer to oxygen molecule.[26,45,46] The electron-transfer number and yield of H_2O_2 can be further calculated through eqs S1 and S2 in the Supporting Information, and the calculated results are illustrated in Figure 4d. In the potential range of 0.2−0.8 V, the electron-transfer number was 3.81−3.95 for $Co(OH)_2$/CoPt/N-CN, comparable with that of Pt/C (3.85−3.86), indicating an ideal four-electron-transfer pathway. Correspondingly, the yield of H_2O_2 was 2.20−9.48%, close to that of Pt/C (6.37−7.16%), suggesting that only very little undesired peroxide intermediates were generated during the ORR process. Furthermore, durability is one of the major concerns in current alkaline fuel cell and Zn−air battery technologies. The amperometric *i*−*t* curves (Figure 4e) show that $Co(OH)_2$/CoPt/N-CN maintained 93% of its initial current density, higher than the Pt/C (∼79%) catalyst after about 11 h of continuous operation at the potential of 0.8 V. Accelerated durability test (ADT) is another important approach to evaluate the long-term stability. ADT measurements were carried out by cycling the catalyst in the potential range of 0.5−1.0 V in O_2-saturated 0.1 mol L^{-1} KOH solution at the scan rate of 50 mV s^{-1} for both $Co(OH)_2$/CoPt/N-CN and Pt/C. As shown in Figure 4f, after 5000 cycles of continuous potential scans, the half-wave potential of $Co(OH)_2$/CoPt/N-CN only shifted 10 mV, however, a 39 mV shift was observed for the Pt/C catalyst. It further attests that the sample of $Co(OH)_2$/CoPt/N-CN had markedly superior long-term durability than Pt/C. The desirable ORR performance of $Co(OH)_2$/CoPt/N-CN is probably ascribed to the CoPt intrinsic activity enhanced by the alloying effects, as well as the well-defined porous structure of N-CN can prevent the coalescence, decomposition, and aggregation of the CoPt nanoparticles and boost the local oxygen concentration on the surface of the CoPt nanoparticles.[24,50]

The OER performance of $Co(OH)_2$/CoPt/N-CN was further examined and compared with the standard IrO_2 catalyst. Figure 5a depicts the OER polarization curves, and at the current density of 10 mA cm^{-2}, $Co(OH)_2$/CoPt/N-CN had an overpotential of 320 mV, outperforming than IrO_2 (350 mV). The Tafel slopes also confirmed this superior OER activity of $Co(OH)_2$/CoPt/N-CN than IrO_2. As shown in Figure 5b, $Co(OH)_2$/CoPt/N-CN afforded a lower Tafel slope (73.4 mV dec^{-1}) close to that of IrO_2 (85.4 mV dec^{-1}), indicating an outstanding OER reaction kinetics. CoPt/$Co(OH)_2$ also exhibited a low Tafel slope value of 76.8 mV dec^{-1}, while in sharp contrast, $Co(OH)_2$ and CoPt/N-CN displayed a much higher Tafel slope of 110.6 and 124.6 mV dec^{-1}, respectively (Figure S10a). To further elucidate the reasons for the outstanding OER performance from $Co(OH)_2$/CoPt/N-CN, the electrochemical impedance test was performed. As shown from the Nyquist plots in Figure 5c, the semicircle at high frequency corresponds to the formation of an electric double layer, and the semicircle at low frequency can be ascribed to the Faradaic reaction of oxygen evolution. $Co(OH)_2$/CoPt/N-CN displayed a much smaller semicircle than IrO_2, and the charge transfer resistance was 31 Ω, much lower than that of IrO_2 (55 Ω). The Nyquist plots of $Co(OH)_2$, CoPt/N-CN, and CoPt/$Co(OH)_2$ can be found in Figure S10b, where all of the samples exhibited a higher charge-transfer resistance than $Co(OH)_2$/CoPt/N-CN. The stability toward OER was then assessed by *i*−*t* chronoamperometric response and presented in Figure 5d. After continuous operation for about 8 h, $Co(OH)_2$/CoPt/N-CN retained 85% of the initial current, while IrO_2 retained only 73% under the same conditions. The combined above results demonstrate that $Co(OH)_2$/CoPt/N-CN had superior OER properties than the IrO_2 catalyst. Such an excellent performance can be accounted for several reasons: first of all, the laminar $Co(OH)_2$

DOI: 10.1021/acsami.8b18424
ACS Appl. Mater. Interfaces 2019, 11, 4983−4994

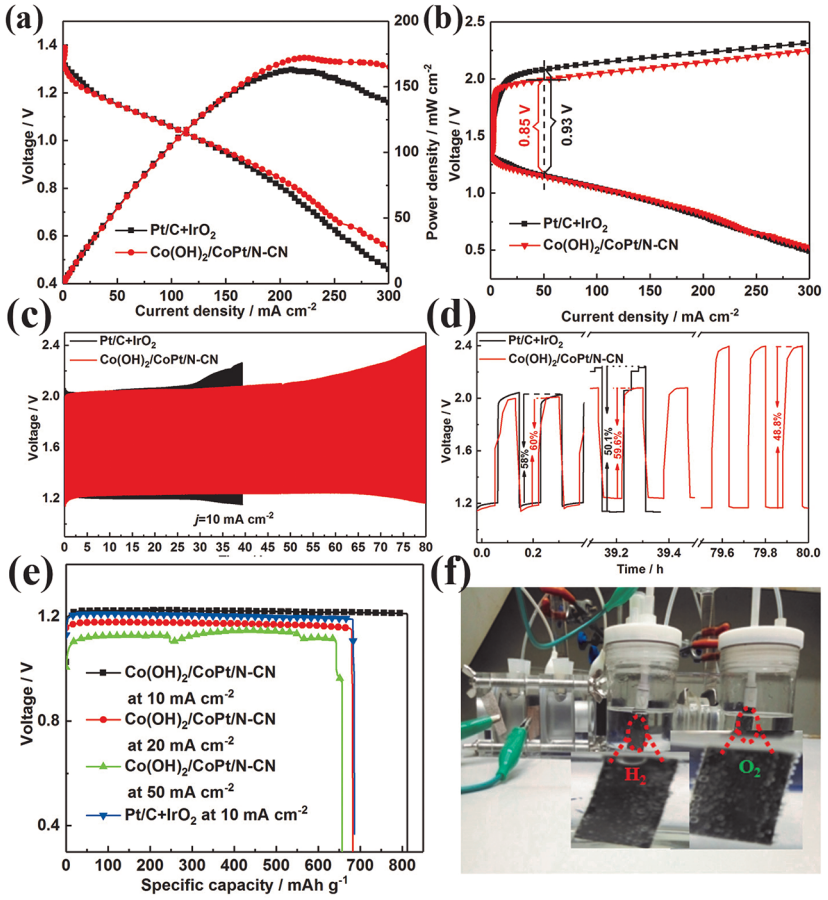

Figure 6. (a) Discharge polarization curves and their corresponding power density curves; (b) charge−discharge polarization curves; (c) galvanostatic charge−discharge test at 10 mA cm^{-2}; (d) round-trip efficiency for galvanostatic charge−discharge test at 10 mA cm^{-2}; (e) specific capacities of $Co(OH)_2$/CoPt/N-CN at 10, 20, 50 mA cm^{-2} and IrO_2 + Pt/C at 10 mA cm^{-2}, (f) two consecutive rechargeable Zn−air batteries as a power for water splitting.

structure possessed high OER catalytic performance;[43,44] second, N-CN intrinsically had good conductivity, and their well-defined mesopore and micropore can facilitate electron transfer and mass transport, as well as increasing the amount of active sites.[18,51]

2.3. Zn−Air Battery Performance. Moving forward for practical applications, the samples were tested as the air−cathode of a self-assembled rechargeable Zn−air battery. As shown in Figures 6a and S11a, the maximal power density of $Co(OH)_2$, CoPt/$Co(OH)_2$, $Co(OH)_2$/CoPt/N-CN, and Pt/C + IrO_2 was 150, 168, 171, and 163 mW cm^{-2}, respectively. The charge−discharge polarization curves (Figures 6b and S11b) revealed that the $Co(OH)_2$/CoPt/N-CN displayed a smaller voltage gap compared with $Co(OH)_2$, CoPt/$Co(OH)_2$, and Pt/C + IrO_2, signifying a much better charge−discharge capability. The stability of air−cathode was then evaluated by continuous galvanostatic charge−discharge at 10 mA cm^{-2} with each cycle of 10 min. As presented in Figures 6c and S11c, the initial voltage gap of $Co(OH)_2$, CoPt/$Co(OH)_2$, $Co(OH)_2$/CoPt/N-CN, and Pt/C + IrO_2 was 0.94, 0.90, 0.82, and 0.83 V, respectively. However, after 30 h, the voltage gap of $Co(OH)_2$ and CoPt/$Co(OH)_2$ increased to 1.23 and 1.04 V, intriguingly, $Co(OH)_2$/CoPt/N-CN and Pt/C + IrO_2 kept a small gap of 0.85 and 0.91 V. When the current density increased to 50 mA cm^{-2} (Figure S12), the $Co(OH)_2$/CoPt/N-CN still maintained a relatively small charge−discharge voltage gap of 0.95 V. As shown in Figure 6d, the round-trip efficiency of $Co(OH)_2$/CoPt/N-CN and Pt/C + IrO_2 was 60 and 58% in the initial charge−discharge process, after 40 h, the round-trip efficiency of Pt/C + IrO_2 has decayed to 50.1%, encouragingly, $Co(OH)_2$/CoPt/N-CN still maintained 58%, and continued to cycle until after 80 h, the round-trip efficiency decayed to 48%. Figure 6f depicts the typical galvanostatic discharge profile at the current density of 10, 20, and 50 mA cm^{-2} for Zn−air battery using $Co(OH)_2$/CoPt/N-CN as the air−cathode. The specific capacity normalized to the weight of consumed zinc plate was 812 mA h g^{-1} at 10 mA cm^{-2}, 682 mA h g^{-1} at 20 mA cm^{-2}, and 656 mA h g^{-1} at 50 mA cm^{-2} for $Co(OH)_2$/CoPt/N-CN; however, the Pt/C + IrO_2 was only 688 mA h g^{-1} at 10 mA cm^{-2}. Figure 6f shows the two-electrode water-splitting device powered by two consecutive rechargeable Zn−air batteries using $Co(OH)_2$/CoPt/N-CN as the air−cathode. The carbon cloth (1 × 2 cm^2) precoated with the $Co(OH)_2$/CoPt/N-CN catalyst was employed as the electrodes (OER and HER) in the water-splitting device, and the catalyst loading mass was 2 mg. One can see that, when the Zn−air batteries were connected, a large number of bubbles (H_2 and O_2, with a bubbling rate of ∼2:1 from bubble observations) overflowed from electrodes. It demonstrated that the rechargeable Zn−air battery using $Co(OH)_2$/CoPt/N-CN as the air−cathode was capable to power the water-splitting device.

Note that, the performance of $Co(OH)_2$/CoPt/N-CN as the air−cathode is at least comparable, if not exceeding, the

DOI: 10.1021/acsami.8b18424
ACS Appl. Mater. Interfaces 2019, 11, 4983−4994

Table 1. Reported Performance of Rechargeable Zn−Air Batteries with Various Bifunctional Electrocatalysts

catalysts	electrolyte	peak power density (mW cm^{-2})	charge−discharge voltage gap (V)	specific capacity (mA h g^{-1})	stability	references
$Co(OH)_2$/CoPt/N-CN	6 M KOH + 0.2 M $Zn(Ac)_2$	171	0.82 at 10 mA cm^{-2}	812 at 10 mA cm^{-2}	10 min/cycle for 300 cycles at 10 mA cm^{-2}, voltage gap increased ∼0.05 V	this work
Co@C−N	6 M KOH + 0.2 M $Zn(Ac)_2$	105	0.82 at 10 mA cm^{-2}	741 at 10 mA cm^{-2}	20 min/cycle for 90 cycles at 10 mA cm^{-2}, voltage gap increased ∼0.02 V	39
Co−N−C	6 M KOH + 0.2 M $ZnCl_2$	152	1.0 at 2 mA cm^{-2}	750 at 20 mA cm^{-2}	20 min/cycle for 180 cycles at 2 mA cm^{-2}, voltage gap increased ∼0.12 V	52
Ag−Cu on Ni foams	6 M KOH + 0.2 M $ZnCl_2$	86	0.96 at 20 mA cm^{-2}	572 at 10 mA cm^{-2}	20 min/cycle for 100 cycles at 20 mA cm^{-2}, negligible change	53
R-CMS/BNC	6 M KOH + 0.2 M $Zn(Ac)_2$	250	0.72 at 20 mA cm^{-2}	550 at 10 mA cm^{-2}	4 h/cycle for 50 cycles at 20 mA cm^{-2}, no significant change	11
Co_4N/CNW/CC	6 M KOH + 0.2 M $Zn(Ac)_2$	174	0.84 at 10 mA cm^{-2}	774 at 10 mA cm^{-2}	20 min/cycle for 408 cycles at 10 mA cm^{-2}, no visible change	54
CuS/NiS_2INs	6 M KOH + 0.2 M $Zn(Ac)_2$	172	0.57 at 25 mA cm^{-2}	678 at 25 mA cm^{-2}	10 min/cycle for 500 cycles at 25 mA cm^{-2}, negligible change	55
Co_3O_4 NS/CC	6 M KOH + 0.2 M $Zn(Ac)_2$	107	0.7 at 5 mA cm^{-2}	535 at 10 mA cm^{-2}	4 min/cycle for 400 cycles at 5 mA cm^{-2}, negligible change	56
3C-900	6 M KOH + 0.2 M $ZnCl_2$	97	0.8 at 5 mA cm^{-2}	727 at 25 mA cm^{-2}	22 min/cycle for 180 cycles at 5 mA cm^{-2}, no voltage drop	57
$Co(OH)_2$ + N-rGO	6 M KOH		1.2 at 15 mA cm^{-2}		40 min/cycle for 75 cycles at 15 mA cm^{-2}, no voltage drop	34

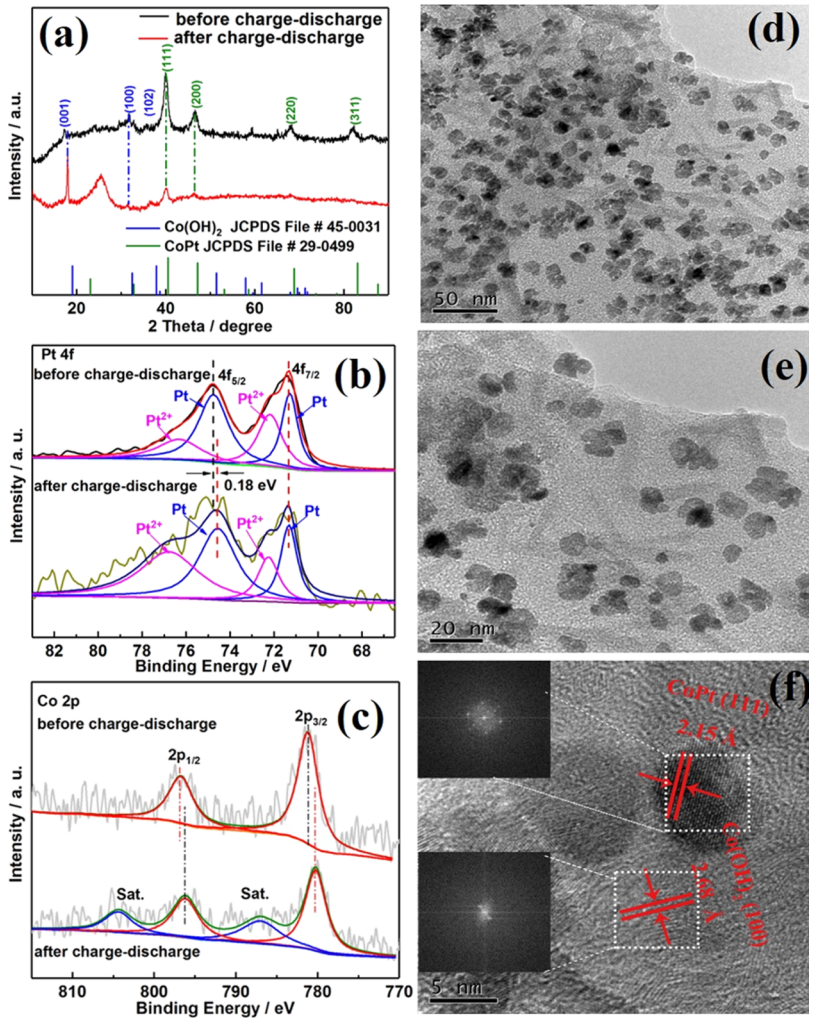

Figure 7. Characterizations before/after the charge−discharge test of $Co(OH)_2$/CoPt/N-CN, (a) XRD patterns, (b) core-level XPS spectra of the Pt 4f electrons and (c) core-level XPS spectra of the Co 2p electrons. (d,e) Typical TEM images of $Co(OH)_2$/CoPt/N-CN after the charge−discharge test. (f) High-resolution TEM and corresponding FFT patterns of $Co(OH)_2$/CoPt/N-CN.

DOI: 10.1021/acsami.8b18424
ACS Appl. Mater. Interfaces 2019, 11, 4983−4994

recently reported electrocatalysts. For comparison, recent results from the literature are summarized in Table 1. For instances, with the same electrolytes employed, the peak power density for $Co(OH)_2$/CoPt/N-CN was higher than Co@C−N,[39] Co−N−C,[52] Ag−Cu on Ni foam,[53] Co_3O_4 NS/CC,[57] and 3C-900.[57] At the current density of 10 mA cm^{-2}, the specific capacity for $Co(OH)_2$/CoPt/N-CN was also larger than all of the above-mentioned materials and Co_4N/CNW/CC,[54] CuS/NiS_2INs,[55] R-CMS/BNC as well,[11] while the charge−discharge gap was also comparable with Co@C−N,[39] Co_4N/CNW/CC[54] and lower than $Co(OH)_2$ + N-rGO.[34] More intriguingly, the long-term stability for $Co(OH)_2$/CoPt/N-CN was in the same level or outperformed than the above composites.

2.4. Structural Characterizations of $Co(OH)_2$/CoPt/N-CN before and after Charge−Discharge. To better understand the reasons for the stability of $Co(OH)_2$/CoPt/N-CN in the Zn−air battery, the structure and composition of $Co(OH)_2$/CoPt/N-CN before and after the charge−discharge test were detected by XRD, XPS, and TEM measurements. Figure S13 presents the XRD patterns of CoPt/N-CN before and after charge−discharge test. It can be recognized that the (111) plane of CoPt nanoparticles exhibited a downshift slightly, indicating that the CoPt/N-CN could not be steady in the electrolyte for Zn−air battery operation. In sharp contrast, no discernible transformation can be observed for the crystal phases of $Co(OH)_2$/CoPt/N-CN (Figure 7a), suggesting an excellent stability upon charge−discharge process. Moreover, the binding energies for the Pt 4f and Co 2p electrons were further probed before and after the charge−discharge test for $Co(OH)_2$/CoPt/N-CN. From Figure 7b, it can be noted that the binding energy of Pt $4f_{5/2}$ decreased slightly with a value of 0.18 eV, indicating the electronic structure of Pt altered during the charge−discharge process. Note that, such binding energy variation is closely related to the shift of d-band center relative to Fermi level, which affects the ORR kinetics eventually.[58] The positive binding energy shift normally signify the downshift of a d-band center, which could weaken the interaction between the oxygenated intermediate and the surface of the catalyst hence promotes the ORR activity. The slight decrease of the binding energy indicates that, the electrocatalytic activity of $Co(OH)_2$/CoPt/N-CN slightly diminished. Moreover, the binding energy of Co 2p electrons (Figure 7c) shifted negatively from 796.9 and 781.0 to 796.3 and 780.4 eV, and the binding energy gap between the $2p_{1/2}$ and $2p_{3/2}$ electrons decreased from 15.9 to 15.8 eV, corroborating a little part of $Co(OH)_2$ was gradually oxidized into Co_3O_4 under prolonged exposure anodic potential region.[34] The above results proved that the foam-like hierarchical structure of $Co(OH)_2$/CoPt/N-CN underwent a minor change in the structural characteristics and chemical composition after long-term charge−discharge test therefore exhibited an excellent stability. Furthermore, the morphology and surface-structure of $Co(OH)_2$/CoPt/N-CN after charge−discharge test was probed by TEM, as shown in Figure 7d,e. Interestingly, the CoPt building blocks remained isolated and individually discernible without aggregation (Figure 7d) upon charge−discharge process. Figure 7e shows the size of the CoPt building block kept almost identical without apparent change. More importantly, in Figure 7f and insert FFT patterns, the lattice spacings of CoPt (2.15 Å) and $Co(OH)_2$ (2.68 Å) remained almost unchanged, further confirming that the hierarchical structure of $Co(OH)_2$/CoPt/N-CN had super-robust long-term stability. Such excellent stability can be probably attributed to the foam-like hierarchical structure, as previous studies have shown that such structure can provide well-defined pores to preserve the active sites and offer ideal pathway for liquid-to-gas (OER process) and gas-to-liquid (ORR process) conversions.[59,60]

These encouraging results have shown the great advantages of $Co(OH)_2$/CoPt/N-CN as an efficient air−cathode for Zn−air battery in terms of high power density, specific capacity and long-term durability. The possible reasons can be ascribed to its unique foam-like structures which impart the following merits: (1) the CoPt alloyed nanoparticles offered desirable intrinsic ORR activity, while $Co(OH)_2$ laminar structure is very active in OER, and the integration of these two endows the composite great electrocatalytic bi-functionalities; (2) the N-CN not only provides excellent conductivity but also offers additional electrochemically active sites for both ORR and OER, and its well-defined porous structure can prevent coalescence, decomposition, and aggregation of the CoPt nanoparticles hence enhance the long-term stability; and (3) most importantly, the three active components can be integrated as a composite with foam-like morphology, in which not only both ORR and OER activities can be simultaneously engineered but also robust stability with super-long cycling life can be achieved.

3. CONCLUSIONS

In summary, an integral composite of $Co(OH)_2$/CoPt/N-CN with excellent ORR and OER dual functionalities as the air−cathode of rechargeable Zn−air battery has been fabricated. Its hierarchical structural features were revealed by multiple techniques, where such a well-defined hierarchical structure imparts the composite with comparable activity and superior durability than Pt/C toward ORR, as well as outperformed OER activity and long-term durability than IrO_2 toward OER. When engineered as the air−cathode for rechargeable Zn−air battery, it shows a high power-density of 171 mW cm^{-2}, a specific capacity of 812 mA h g^{-1}, and a robust cycle life. Using $Co(OH)_2$/CoPt/N-CN as air−cathode, we demonstrate that two consecutive Zn−air batteries can power a water splitting device. This work enriches the toolbox for the design and construction of more cost-effective bi-functional electrocatalysts for metal−air battery systems.

4. EXPERIMENTAL SECTION

4.1. Materials. Sodium chloride (NaCl), cobalt nitrate hexahydrate ($Co(NO_3)_2{\cdot}6H_2O$), glucose, and urea were purchased from Guangzhou Chemical Reagent Factory (Guangzhou, China). Sodium borohydride ($NaBH_4$), zinc acetate ($Zn(Ac)_2{\cdot}2H_2O$), potassium hydroxide (KOH), L-ascorbic acid (L-AA), and chloroplatinic acid hexahydrate ($H_2PtCl_6{\cdot}6H_2O$) were obtained from Energy Chemicals (Shanghai, China). Iridium oxide (IrO_2) and commercial 20% Pt/C were acquired from Alfa Aesar. All aqueous solutions were prepared using deionized water with a resistivity of 18.3 MΩ·cm.

4.2. Preparation of Nitrogen-Doped Carbon Nanosheets (Denoted as N-CN). Nitrogen-doped porous carbon was synthesized by following Scheme 1. In a typical preparation,[61] One gram of glucose, 1 g of urea, and 20 g of NaCl were first co-dissolved in 60 mL deionized water, freezing-dried at −50 °C under vacuum, and then manually grinded in an agate mortar for 20 min. Subsequently, the obtained sample was carbonized at 300 °C for 1 h, and then 800 °C for 1 h (heating rate 2 °C min^{-1}) under Ar atmosphere with a steam rate of 20 sccm. Once cooled down to room temperature, the sample was dissolved in deionized water and filtered to remove NaCl. Finally,

DOI: 10.1021/acsami.8b18424
ACS Appl. Mater. Interfaces 2019, 11, 4983−4994

240 mg of N-CN sample was obtained by drying at 35 °C in a vacuum oven for 12 h.

4.3. Preparation of $Co(OH)_2$ Nanosheets. $Co(OH)_2$ nanosheets were synthesized through the following approach: typically, 20 mL of KOH (0.27 M) aqueous solution was dropwise added into 60 mL of $Co(NO_3)_2{\cdot}6H_2O$ (0.025 M) and L-AA (0.01 M) mixed aqueous solution. After stirring at 40 °C for 4 h, the above solution was transferred into a 100 mL Teflon-lined stainless-steel autoclave and heated at 180 °C for 24 h. Followed by cooling down at room temperature, the sample was washed with deionized water and dried at 35 °C for 12 h in the vacuum oven. The collected solid was the $Co(OH)_2$ nanosheets. The yield of $Co(OH)_2$ is ∼86%.

4.4. Preparation of CoPt/N-CN and CoPt/$Co(OH)_2$. CoPt/N-CN was synthesized by an in situ reduction method (Scheme 1). To achieve this, 0.1 mmol $H_2PtCl_6{\cdot}6H_2O$ and 0.033 mmol $Co(NO_3)_2{\cdot}6H_2O$ were co-dissolved in 10 mL of deionized water, and then the dispersed 180 mg N-CN sample was added into the above solution under stirring for 4 h to ensure that Co^{2+} and Pt^{4+} were fully adsorbed into the pores of N-CN. Subsequently, 20 mL of $NaBH_4$ (30 mmol L^{-1}) was added dropwise into the mixture under a constant stirring for 6 h at 40 °C. Finally, the sample was washed with deionized water and dried at 35 °C in a vacuum oven (the yield of CoPt/N-CN is ∼92%). CoPt/$Co(OH)_2$ electrocatalysts were prepared in a similar manner by replacing N-CN with $Co(OH)_2$ while the weight percentage of CoPt remained unchanged (the yield of CoPt/$Co(OH)_2$ is ∼92%). The method for preparing Co/N-CN is same as that for CoPt/N-CN without adding Pt precursor (the yield of Co/N-CN is ∼93%).

4.5. Preparation of $Co(OH)_2$/CoPt/N-CN. The $Co(OH)_2$/CoPt/N-CN sample was prepared through a two-step process (Scheme 1). Typically, the CoPt/N-CN was first prepared by following the above method. CoPt/N-CN was then dispersed into 10 mL of deionized water and ultrasonicated for 5 min, while 1 mmol $Co(NO_3)_2{\cdot}6H_2O$ and 0.4 mmol LAA acid were co-dissolved in 20 mL of deionized water and added into the CoPt/N-CN dispersion. Subsequently, 30 mL of KOH (0.15 mol L^{-1}) aqueous solution was added into the above mixed solution dropwise and kept stirring for 4 h at 40 °C. Then, the mixture was transferred into a 100 mL Teflon-lined stainless-steel autoclave and heated at 180 °C for 24 h. Followed by cooling down at room temperature, the sample was washed with deionized water and dried at 35 °C for 12 h in the vacuum oven. The collected solid was the $Co(OH)_2$/CoPt/N-CN sample (the yield of $Co(OH)_2$/CoPt/N-CN is ∼90%). The physical mixture of $Co(OH)_2$, CoPt and N-CN was prepared by ultrasonically dispersing $Co(OH)_2$, CoPt, and N-CN with 0.01% Nafion solution for 30 min.

4.6. Electrochemical Measurements. Electrochemical measurements were carried out via a CHI 760E electrochemical workstation (CH Instruments) within a three-electrode cell and rotating ring disk electrode (Pine Instruments) under ambient conditions. The working electrode was prepared by drop-casting a catalyst ink on a prepolished glass carbon electrode (GCE, 5 mm in diameter). To prepare homogeneous catalyst ink, 2 mg of as-synthesized sample was dispersed into 0.4 mL of Nafion/ethanol (the weight percentage of Nafion is 0.05%) solution under ultrasonic treatment for 30 min, and then 4 μL of above catalyst ink was drop-casted onto GCE and dried at ambient temperature (the loading of catalyst on GCE was 102 μg cm^{-2}). A platinum plate (1.5 cm × 1.5 cm) was used as the counter electrode, and the Ag/AgCl with saturated KCl was employed as the reference electrode. All potentials were converted to a reversible hydrogen electrode (RHE) via the equation of the $E_{RHE} = E_{Ag/AgCl} + 0.196 + 0.059 \times pH$. The ORR activities were evaluated by linear sweep voltammetry (LSV) and cyclic voltammetry (CV) with the potential ranging from −1 to 0.2 V (vs Ag/AgCl) at a scan rate of 10 mV s^{-1} under different rotation rates (400, 625, 900, 1225, 1600, 2025, and 2500 rpm) in a O_2-saturated 0.1 mol L^{-1} KOH electrolyte. The durability was performed via the amperometric i−t curve in O_2-saturated 0.1 mol L^{-1} KOH electrolyte with the rotation speed of 900 rpm at potential of 0.5 V for 30 000 s. The OER performance was tested using LSV at a scan rate of 10 mV s^{-1} with 1600 rpm rotation speed in N_2-saturated 1 mol L^{-1} KOH solution. Electrochemical impedance spectra of OER were conducted on the GCE at 1.55 V (vs RHE) with the ac amplitude of 5 mV with the frequency ranging from 100 kHz to 0.01 Hz in N_2-saturated 1 mol L^{-1} KOH solution.

4.7. Rechargeable Zn−Air Battery. A rechargeable Zn−air battery was self-assembled by adopting a zinc plate as the anode, while the dual-functional catalyst loaded on hydrophobic carbon cloth was employed as the air−cathode and diffusion layer. The air−cathode was fabricated by the following method: 2 mg of catalyst was first dispersed into 400 μL of Nafion solution (0.5 wt %) and subject to ultrasonic treatment for 30 min, and then, the above mixture was drop-casted onto the hydrophobic side of the carbon cloth, ensuring the effective catalyst geometric area was 1 cm^2 (the catalyst loading was 2 mg cm^{-2}). The electrolyte employed was 6 M KOH and 0.2 M $Zn(Ac)_2{\cdot}2H_2O$. The galvanostatic charge−discharge and discharge capacity measurements were performed by LAND CT2001A battery program-control test system. The discharge and charge polarization curves were recorded by CHI 760E working station.

4.8. Characterization. The morphology and surface structure of the samples were observed by a high-resolution transmission electron microscope (HRTEM, JEOL-2010, operated at 200 kV) and field-emission scanning electron microscope (SEM, Merlin, operated at 10 kV). The crystal structural feature of the electrocatalysts was identified by XRD (Empyrean) with Cu Kα (λ = 1.5406 Å) radiation at a scanning rate of $2\theta = 2°$ min^{-1}. XPS were recorded on a Phi X-tool instrument with an Al Kα ($h\nu$ = 1486.6 eV) source. An incident X-ray beam was focused on an analysis area of 200 μm in diameter with the take-off angle of 45° to the sample surface, and the pass energy is 55.0 eV with the energy step of 0.1 eV. The charge correction was performed the carbon C 1s peak at 285 eV as the reference value. The specific surface area and the pore size distribution of the samples were estimated from nitrogen adsorption isotherm (Quantachrome Autosorb-iQ instrument at 77 K) by means of the BET equation and the Barrett−Joyner−Halenda model. FT-IR was conducted on Nicolet 6700 with the wavenumber of 400−4000 cm^{-1}. The detection mode is the transmission ESP, the spectra were collected at 32 scans with a spectral resolution of 4 cm^{-1}. The Raman spectra measurement was performed using a laser Raman spectrometer (Jobin Yvon, model T6400).

■ ASSOCIATED CONTENT

Supporting Information

The Supporting Information is available free of charge on the ACS Publications website at DOI: 10.1021/acsami.8b18424.

SEM image, N_2 adsorption−desorption curves, FT-IR spectra, Raman spectra, LSV curves, additional Tafel plots and electrochemical impedance spectra, and additional XRD spectra (PDF)

■ AUTHOR INFORMATION

Corresponding Authors

*E-mail: zhht@scut.edu.cn (Z.T.).
*E-mail: n.bedford@unsw.edu.au (N.M.B.).

ORCID

Zhenghua Tang: 0000-0003-0718-3164
Ligui Li: 0000-0002-1636-9342
Shaowei Chen: 0000-0002-3668-8551
Nicholas M. Bedford: 0000-0002-4424-7094

Author Contributions

The manuscript was written through contributions of all authors. All authors have given approval to the final version of the manuscript.

Notes

The authors declare no competing financial interest.

DOI: 10.1021/acsami.8b18424
ACS Appl. Mater. Interfaces 2019, 11, 4983−4994

■ ACKNOWLEDGMENTS

Z.T. acknowledges the financial support from the National Natural Science Foundation of China (no. 21501059), Guangzhou Science and Technology Plan Projects (no. 201804010323), Guangdong Natural Science Funds for Distinguished Young Scholars (no. 2015A030306006), Science and Technology Program of Guangdong Province (no. 2017A050506014), and Guangdong Innovative and Entrepreneurial Research Team Program (no. 2014ZT05N200).

■ REFERENCES

(1) Li, Y.; Lu, J. Metal-Air Batteries: Will They Be the Future Electrochemical Energy Storage Device of Choice? *ACS Energy Lett.* **2017**, *2*, 1370−1377.
(2) Li, Y.; Dai, H. Recent Advances in Zinc-Air Batteries. *Chem. Soc. Rev.* **2014**, *43*, 5257−5275.
(3) Guan, C.; Sumboja, A.; Wu, H.; Ren, W.; Liu, X.; Zhang, H.; Liu, Z.; Cheng, C.; Pennycook, S. J.; Wang, J. Hollow Co3 O4 Nanosphere Embedded in Carbon Arrays for Stable and Flexible Solid-State Zinc-Air Batteries. *Adv. Mater.* **2017**, *29*, 1704117.
(4) Cai, X.; Lai, L.; Lin, J.; Shen, Z. Recent Advances in Air Electrodes for Zn-Air Batteries: Electrocatalysis and Structural Design. *Mater. Horiz.* **2017**, *4*, 945−976.
(5) Yin, J.; Li, Y.; Lv, F.; Fan, Q.; Zhao, Y.-Q.; Zhang, Q.; Wang, W.; Cheng, F.; Xi, P.; Guo, S. NiO/CoN Porous Nanowires as Efficient Bifunctional Catalysts for Zn-Air Batteries. *ACS Nano* **2017**, *11*, 2275−2283.
(6) Yin, J.; Li, Y.; Lv, F.; Lu, M.; Sun, K.; Wang, W.; Wang, L.; Cheng, F.; Li, Y.; Xi, P.; Guo, S. Oxygen Vacancies Dominated NiS2 /CoS2 Interface Porous Nanowires for Portable Zn-Air Batteries Driven Water Splitting Devices. *Adv. Mater.* **2017**, *29*, 1704681.
(7) Wang, Q.; Lei, Y.; Chen, Z.; Wu, N.; Wang, Y.; Wang, B.; Wang, Y. Fe/Fe3C@C Nanoparticles Encapsulated in N-doped Graphene-CNTs Framework as an Efficient Bifunctional Oxygen Electrocatalyst for Robust Rechargeable Zn-Air Batteries. *J. Mater. Chem. A* **2018**, *6*, 516−526.
(8) Wang, X.; Li, Y.; Jin, T.; Meng, J.; Jiao, L.; Zhu, M.; Chen, J. Electrospun Thin-Walled CuCo2O4@C Nanotubes as Bifunctional Oxygen Electrocatalysts for Rechargeable Zn-Air Batteries. *Nano Lett.* **2017**, *17*, 7989−7994.
(9) Lee, D. U.; Xu, P.; Cano, Z. P.; Kashkooli, A. G.; Park, M. G.; Chen, Z. Recent progress and perspectives on bi-functional oxygen electrocatalysts for advanced rechargeable metal-air batteries. *J. Mater. Chem. A* **2016**, *4*, 7107−7134.
(10) Liu, W.; Zhang, J.; Bai, Z.; Jiang, G.; Li, M.; Feng, K.; Yang, L.; Ding, Y.; Yu, T.; Chen, Z.; Yu, A. Controllable Urchin-Like NiCo2 S4 Microsphere Synergized with Sulfur-Doped Graphene as Bifunctional Catalyst for Superior Rechargeable Zn-Air Battery. *Adv. Funct. Mater.* **2018**, *28*, 1706675.
(11) Wang, Z.; Xiao, S.; An, Y.; Long, X.; Zheng, X.; Lu, X.; Tong, Y.; Yang, S. Co(II)1-xCo(0)x/3Mn(III)2x/3S Nanoparticles Supported on B/N-Codoped Mesoporous Nanocarbon as a Bifunctional Electrocatalyst of Oxygen Reduction/Evolution for High-Performance Zinc-Air Batteries. *ACS Appl. Mater. Interfaces* **2016**, *8*, 13348−13359.
(12) Fan, K.; Chen, H.; Ji, Y.; Huang, H.; Claesson, P. M.; Daniel, Q.; Philippe, B.; Rensmo, H.; Li, F.; Luo, Y.; Sun, L. Nickel−Vanadium Monolayer Double Hydroxide for Efficient Electrochemical Water Oxidation. *Nat. Commun.* **2016**, *7*, 11981.
(13) Song, F.; Hu, X. Ultrathin Cobalt-Manganese Layered Double Hydroxide Is an Efficient Oxygen Evolution Catalyst. *J. Am. Chem. Soc.* **2014**, *136*, 16481−16484.
(14) Nai, J.; Yin, H.; You, T.; Zheng, L.; Zhang, J.; Wang, P.; Jin, Z.; Tian, Y.; Liu, J.; Tang, Z.; Guo, L. Efficient Electrocatalytic Water Oxidation by Using Amorphous Ni-Co Double Hydroxides Nanocages. *Adv. Energy Mater.* **2015**, *5*, 1401880.
(15) Song, F.; Hu, X. Exfoliation of Layered Double Hydroxides for Enhanced Oxygen Evolution Catalysis. *Nat. Commun.* **2014**, *5*, 4477.
(16) Burke, M. S.; Kast, M. G.; Trotochaud, L.; Smith, A. M.; Boettcher, S. W. Cobalt-Iron (Oxy)hydroxide Oxygen Evolution Electrocatalysts: The Role of Structure and Composition on Activity, Stability, and Mechanism. *J. Am. Chem. Soc.* **2015**, *137*, 3638−3648.
(17) Morales-Guio, C. G.; Liardet, L.; Hu, X. Oxidatively Electrodeposited Thin-Film Transition Metal (Oxy)hydroxides as Oxygen Evolution Catalysts. *J. Am. Chem. Soc.* **2016**, *138*, 8946−8957.
(18) Wang, Q.; Shang, L.; Shi, R.; Zhang, X.; Zhao, Y.; Waterhouse, G. I. N.; Wu, L.-Z.; Tung, C.-H.; Zhang, T. NiFe Layered Double Hydroxide Nanoparticles on Co,N-Codoped Carbon Nanoframes as Efficient Bifunctional Catalysts for Rechargeable Zinc-Air Batteries. *Adv. Energy Mater.* **2017**, *7*, 1700467.
(19) Sumboja, A.; Chen, J.; Zong, Y.; Lee, P. S.; Liu, Z. NiMn layered double hydroxides as efficient electrocatalysts for the oxygen evolution reaction and their application in rechargeable Zn-air batteries. *Nanoscale* **2017**, *9*, 774−780.
(20) Huang, X.; Zhao, Z.; Cao, L.; Chen, Y.; Zhu, E.; Lin, Z.; Li, M.; Yan, A.; Zettl, A.; Wang, Y. M.; Duan, X.; Mueller, T.; Huang, Y. High-performance Transition Metal−doped Pt_3Ni Octahedra for Oxygen Reduction Reaction. *Science* **2015**, *348*, 1230−1234.
(21) Bu, L.; Zhang, N.; Guo, S.; Zhang, X.; Li, J.; Yao, J.; Wu, T.; Lu, G.; Ma, J.-Y.; Su, D.; Huang, X. Biaxially Strained PtPb/Pt Core/shell Nanoplate Boosts Oxygen Reduction Catalysis. *Science* **2016**, *354*, 1410−1414.
(22) Wang, C.; Markovic, N. M.; Stamenkovic, V. R. Advanced Platinum Alloy Electrocatalysts for the Oxygen Reduction Reaction. *ACS Catal.* **2012**, *2*, 891−898.
(23) Stamenkovic, V.; Mun, B. S.; Mayrhofer, K. J. J.; Ross, P. N.; Markovic, N. M.; Rossmeisl, J.; Greeley, J.; Nørskov, J. K. Changing the Activity of Electrocatalysts for Oxygen Reduction by Tuning the Surface Electronic Structure. *Angew. Chem., Int. Ed.* **2006**, *45*, 2897−2901.
(24) Choi, S.-I.; Lee, S.-U.; Kim, W. Y.; Choi, R.; Hong, K.; Nam, K. M.; Han, S. W.; Park, J. T. Composition-Controlled PtCo Alloy Nanocubes with Tuned Electrocatalytic Activity for Oxygen Reduction. *ACS Appl. Mater. Interfaces* **2012**, *4*, 6228−6234.
(25) Alia, S. M.; Pylypenko, S.; Neyerlin, K. C.; Cullen, D. A.; Kocha, S. S.; Pivovar, B. S. Platinum-Coated Cobalt Nanowires as Oxygen Reduction Reaction Electrocatalysts. *ACS Catal.* **2014**, *4*, 2680−2686.
(26) Wang, L.; Tang, Z.; Yan, W.; Wang, Q.; Yang, H.; Chen, S. Co@Pt Core@Shell Nanoparticles Encapsulated in Porous Carbon Derived From Zeolitic Imidazolate Framework 67 for Oxygen Electroreduction in Alkaline Media. *J. Power Sources* **2017**, *343*, 458−466.
(27) Wan, G.; Ma, M.; Jia, A.; Chen, L.; Chen, Y.; Cui, X.; Chen, H.; Shi, J. A 3D Hierarchical Assembly of Optimized Heterogeneous Carbon Nanosheets for Highly Efficient Electrocatalysis. *J. Mater. Chem. A* **2016**, *4*, 11625−11629.
(28) Wang, H.; Wang, W.; Asif, M.; Yu, Y.; Wang, Z.; Wang, J.; Liu, H.; Xiao, J. Cobalt Ion-coordinated Self-assembly Synthesis of Nitrogen-doped Ordered Mesoporous Carbon Nanosheets for Efficiently Catalyzing Oxygen Reduction. *Nanoscale* **2017**, *9*, 15534−15541.
(29) Wei, W.; Liang, H.; Parvez, K.; Zhuang, X.; Feng, X.; Müllen, K. Nitrogen-Doped Carbon Nanosheets with Size-Defined Mesopores as Highly Efficient Metal-Free Catalyst for the Oxygen Reduction Reaction. *Angew. Chem., Int. Ed.* **2014**, *53*, 1570−1574.
(30) Zhao, Y.; Ma, H.; Huang, S.; Zhang, X.; Xia, M.; Tang, Y.; Ma, Z.-F. Monolayer Nickel Cobalt Hydroxyl Carbonate for High Performance All-Solid-State Asymmetric Supercapacitors. *ACS Appl. Mater. Interfaces* **2016**, *8*, 22997−23005.
(31) Zhao, L.; Sui, X.-L.; Li, J.-L.; Zhang, J.-J.; Zhang, L.-M.; Wang, Z.-B. 3D Hierarchical Pt-Nitrogen-Doped-Graphene-Carbonized Commercially Available Sponge as a Superior Electrocatalyst for Low-Temperature Fuel Cells. *ACS Appl. Mater. Interfaces* **2016**, *8*, 16026−16034.
(32) Xiong, P.; Huang, H.; Wang, X. Design and Synthesis of Ternary Cobalt Ferrite/Graphene/Polyaniline Hierarchical Nano-

DOI: 10.1021/acsami.8b18424
ACS Appl. Mater. Interfaces 2019, 11, 4983−4994

composites for High-performance Supercapacitors. *J. Power Sources* **2014**, *245*, 937−946.
(33) Wang, Y.; Liu, Q.; Sun, Y.; Wang, R. Magnetic field modulated SERS enhancement of CoPt hollow nanoparticles with sizes below 10 nm. *Nanoscale* **2018**, *10*, 12650−12656.
(34) Zhan, Y.; Du, G.; Yang, S.; Xu, C.; Lu, M.; Liu, Z.; Lee, J. Y. Development of Cobalt Hydroxide as a Bifunctional Catalyst for Oxygen Electrocatalysis in Alkaline Solution. *ACS Appl. Mater. Interfaces* **2015**, *7*, 12930−12936.
(35) Gaikar, P. S.; Navale, S. T.; Gaikwad, S. L.; Al-Osta, A.; Jadhav, V. V.; Arjunwadkar, P. R.; Naushad, M.; Mane, R. S. Pseudocapacitive performance of a solution-processed β-Co(OH)2 electrode monitored through its surface morphology and area. *Dalton Trans.* **2017**, *46*, 3393−3399.
(36) Nagaraju, G.; Raju, G. S. R.; Ko, Y. H.; Yu, J. S. Hierarchical Ni-Co Layered Double Hydroxide Nanosheets Entrapped on Conductive Textile Fibers: a Cost-Effective and Flexible Electrode For High-performance Pseudocapacitors. *Nanoscale* **2016**, *8*, 812−825.
(37) Liu, X.; Amiinu, I. S.; Liu, S.; Cheng, K.; Mu, S. Transition Metal/nitrogen Dual-doped Mesoporous Graphene-like Carbon Nanosheets For the Oxygen Reduction and Evolution Reactions. *Nanoscale* **2016**, *8*, 13311−13320.
(38) Zhang, F.; Yuan, C.; Lu, X.; Zhang, L.; Che, Q.; Zhang, X. Facile Growth of Mesoporous Co3O4 Nanowire Arrays on Ni Foam for High Performance Electrochemical Capacitors. *J. Power Sources* **2012**, *203*, 250−256.
(39) Zhang, M.; Dai, Q.; Zheng, H.; Chen, M.; Dai, L. Novel MOF-Derived Co@N-C Bifunctional Catalysts for Highly Efficient Zn-Air Batteries and Water Splitting. *Adv. Mater.* **2018**, *30*, 1705431−1705441.
(40) Huang, L.; Jiang, J.; Ai, L. Interlayer Expansion of Layered Cobalt Hydroxide Nanobelts to Highly Improve Oxygen Evolution Electrocatalysis. *ACS Appl. Mater. Interfaces* **2017**, *9*, 7059−7067.
(41) Zhao, Y.; Liu, J.; Zhao, Y.; Wang, F.; Song, Y. Pt-Co Secondary Solid Solution Nanocrystals Supported on Carbon as Next-Generation Catalysts for the Oxygen Reduction Reaction. *J. Mater. Chem. A* **2015**, *3*, 20086−20091.
(42) Tan, B. J.; Klabunde, K. J.; Sherwood, P. M. A. XPS Studies of Solvated Metal Atom Dispersed (SMAD) Catalysts. Evidence for Layered Cobalt-Manganese Particles on Alumina and Silica. *J. Am. Chem. Soc.* **1991**, *113*, 855−861.
(43) Yang, H.; Long, Y.; Zhu, Y.; Zhao, Z.; Ma, P.; Jin, J.; Ma, J. Crystal Lattice Distortion in Ultrathin Co(OH)2 Nanosheets Inducing Elongated Co-OOH Bonds for Highly Efficient Oxygen Evolution Reaction. *Green Chem.* **2017**, *19*, 5809−5817.
(44) Wang, Y.; Zhang, Y.; Liu, Z.; Xie, C.; Feng, S.; Liu, D.; Shao, M.; Wang, S. Layered Double Hydroxide Nanosheets with Multiple Vacancies Obtained by Dry Exfoliation as Highly Efficient Oxygen Evolution Electrocatalysts. *Angew. Chem., Int. Ed.* **2017**, *56*, 5867−5871.
(45) Wang, L.; Tang, Z.; Yan, W.; Yang, H.; Wang, Q.; Chen, S. Porous Carbon-Supported Gold Nanoparticles for Oxygen Reduction Reaction: Effects of Nanoparticle Size. *ACS Appl. Mater. Interfaces* **2016**, *8*, 20635−20641.
(46) Wu, W.; Tang, Z.; Wang, K.; Liu, Z.; Li, L.; Chen, S. Peptide Templated AuPt Alloyed Nanoparticles as Highly Efficient Bifunctional Electrocatalysts for both Oxygen Reduction Reaction and Hydrogen Evolution Reaction. *Electrochim. Acta* **2018**, *260*, 168−176.
(47) He, G.; Song, Y.; Liu, K.; Walter, A.; Chen, S.; Chen, S. Oxygen Reduction Catalyzed by Platinum Nanoparticles Supported on Graphene Quantum Dots. *ACS Catal.* **2013**, *3*, 831−838.
(48) Liu, M.; Zhang, R.; Chen, W. Graphene-Supported Nanoelectrocatalysts for Fuel Cells: Synthesis, Properties, and Applications. *Chem. Rev.* **2014**, *114*, 5117−5160.
(49) Shao, M.; Chang, Q.; Dodelet, J.-P.; Chenitz, R. Recent Advances in Electrocatalysts for Oxygen Reduction Reaction. *Chem. Rev.* **2016**, *116*, 3594−3657.
(50) Choi, D. S.; Robertson, A. W.; Warner, J. H.; Kim, S. O.; Kim, H. Low-Temperature Chemical Vapor Deposition Synthesis of Pt-Co Alloyed Nanoparticles with Enhanced Oxygen Reduction Reaction Catalysis. *Adv. Mater.* **2016**, *28*, 7115−7122.
(51) Wang, T.; Kou, Z.; Mu, S.; Liu, J.; He, D.; Amiinu, I. S.; Meng, W.; Zhou, K.; Luo, Z.; Chaemchuen, S.; Verpoort, F. 2D Dual-Metal Zeolitic-Imidazolate-Framework-(ZIF)-Derived Bifunctional Air Electrodes with Ultrahigh Electrochemical Properties for Rechargeable Zinc-Air Batteries. *Adv. Funct. Mater.* **2018**, *28*, 1705048.
(52) Tang, C.; Wang, B.; Wang, H.-F.; Zhang, Q. Defect Engineering toward Atomic Co-N x -C in Hierarchical Graphene for Rechargeable Flexible Solid Zn-Air Batteries. *Adv. Mater.* **2017**, *29*, 1703185.
(53) Jin, Y.; Chen, F. Facile Preparation of Ag-Cu Bifunctional Electrocatalysts for Zinc-Air Batteries. *Electrochim. Acta* **2015**, *158*, 437−445.
(54) Meng, F.; Zhong, H.; Bao, D.; Yan, J.; Zhang, X. In Situ Coupling of Strung Co4N and Intertwined N-C Fibers toward Free-Standing Bifunctional Cathode for Robust, Efficient, and Flexible Zn-Air Batteries. *J. Am. Chem. Soc.* **2016**, *138*, 10226−10231.
(55) An, L.; Li, Y.; Luo, M.; Yin, J.; Zhao, Y.-Q.; Xu, C.; Cheng, F.; Yang, Y.; Xi, P.; Guo, S. Atomic-Level Coupled Interfaces and Lattice Distortion on CuS/NiS2 Nanocrystals Boost Oxygen Catalysis for Flexible Zn-Air Batteries. *Adv. Funct. Mater.* **2017**, *27*, 1703779.
(56) Song, Z.; Han, X.; Deng, Y.; Zhao, N.; Hu, W.; Zhong, C. Clarifying the Controversial Catalytic Performance of Co(OH)2 and Co3O4 for Oxygen Reduction/Evolution Reactions toward Efficient Zn-Air Batteries. *ACS Appl. Mater. Interfaces* **2017**, *9*, 22694−22703.
(57) Li, T.; Lu, Y.; Zhao, S.; Gao, Z.-D.; Song, Y.-Y. Co3O4-doped Co/CoFe Nanoparticles Encapsulated in Carbon Shells as Bifunctional Electrocatalysts for Rechargeable Zn-Air Batteries. *J. Mater. Chem. A* **2018**, *6*, 3730−3737.
(58) Kitchin, J. R.; Nørskov, J. K.; Barteau, M. A.; Chen, J. G. Modification of the surface electronic and chemical properties of Pt(111) by subsurface 3d transition metals. *J. Chem. Phys.* **2004**, *120*, 10240−10246.
(59) Deng, J.; Li, H.; Wang, S.; Ding, D.; Chen, M.; Liu, C.; Tian, Z.; Novoselov, K. S.; Ma, C.; Deng, D.; Bao, X. Multiscale Structural and Electronic Control of Molybdenum Disulfide Foam for Highly Efficient Hydrogen Production. *Nat. Commun.* **2017**, *8*, 14430.
(60) Fang, Z.; Peng, L.; Qian, Y.; Zhang, X.; Xie, Y.; Cha, J. J.; Yu, G. Dual Tuning of Ni-Co-A (A = P, Se, O) Nanosheets by Anion Substitution and Holey Engineering for Efficient Hydrogen Evolution. *J. Am. Chem. Soc.* **2018**, *140*, 5241−5247.
(61) Zhu, S.; Li, J.; Deng, X.; He, C.; Liu, E.; He, F.; Shi, C.; Zhao, N. Ultrathin-Nanosheet-Induced Synthesis of 3D Transition Metal Oxides Networks for Lithium Ion Battery Anodes. *Adv. Funct. Mater.* **2017**, *27*, 1605017.

DOI: 10.1021/acsami.8b18424
ACS Appl. Mater. Interfaces 2019, 11, 4983−4994